Materials Horizons

A quadruple-band metal-nitride nanowire artificial photosynthesis system for high efficiency photocatalytic overall solar water splitting

Journal:	*Materials Horizons*
Manuscript ID	MH-COM-02-2019-000257.R1
Article Type:	Communication
Date Submitted by the Author:	20-Mar-2019
Complete List of Authors:	Wang, Yongjie; University of Michigan, EECS Wu, Yuanpeng; University of Michigan, EECS Sun, Kai; University of Michigan, Materials Science and Engineering Mi, Zetian; University of Michigan

Conceptual insights

Photocatalytic overall water splitting has been considered as one of the most promising approaches of renewable energy production and environmental remediation, which can perform one-step dissociation of water in nearly pH neutral solution. To date, however, the best reported solar-to-hydrogen conversion efficiency for pH neutral photocatalytic water splitting is limited to ~1-2%, or less, mainly due to insufficient solar absorption and charge carrier separation. In this work, we have investigated the design, synthesis, and characterization of quadruple-band InGaN nanowire arrays for high efficiency overall solar water splitting, which can harvest solar photons in the entire visible spectrum. Significantly, the InGaN nanowires are characterized by the presence of well-defined anode and cathode surfaces for water oxidation and proton reduction, respectively, which enable a precise control of charge carrier flow at the nanoscale. The spatially separated electron and hole gas significantly minimizes surface and bulk recombination and suppresses back reaction, which have been some of the major challenges for achieving efficient photocatalytic water splitting to date.

A quadruple-band metal-nitride nanowire artificial photosynthesis system for high efficiency photocatalytic overall solar water splitting

Yongjie Wang[1], Yuanpeng Wu[1], Kai Sun[2], and Zetian Mi[1,*]

[1]*Department of Electrical Engineering and Computer Science, University of Michigan, 1301 Beal Avenue, Ann Arbor, Michigan 48109, USA*

[2]*Department of Materials Science and Engineering, University of Michigan, 2300 Hayward Street, Ann Arbor, Michigan 48109, USA*

[*]*Corresponding author: ztmi@umich.edu*

ABSTRACT

Photocatalytic water splitting is a wireless method for solar-to-hydrogen conversion. To date, however, the efficiency of photocatalytic water splitting is still very low. Here, we have investigated the design, synthesis, and characterization of quadruple-band InGaN nanowire arrays, which consist of $In_{0.35}Ga_{0.65}N$, $In_{0.27}Ga_{0.73}N$, $In_{0.20}Ga_{0.80}N$, and GaN segments, with energy bandgaps ~2.1 eV, 2.4 eV, 2.6 eV, and 3.4 eV, respectively. Such multi-band InGaN nanowire arrays are integrated directly on a nonplanar wafer for enhanced light absorption. Moreover, a doping gradient is introduced along the lateral dimension of the nanowires, which forms a built-in electric field and promotes efficient charge carrier separation and extraction for water redox reactions. We have demonstrated that the quadruple-band InGaN nanowire photocatalyst can exhibit a solar-to-hydrogen efficiency of ~5.2% with relatively stable operation. This work demonstrates a novel strategy using multi-band semiconductor nanostructures for artificial photosynthesis and solar fuel conversion with significantly improved performance.

Photocatalytic water splitting is a wireless approach to convert solar energy directly to hydrogen fuels, which is an essential step of artificial photosynthesis.[1-4] Unlike photoelectrochemical water splitting that generally requires the integration of two (photo)electrodes in highly conductive electrolyte, water redox reactions can occur on the same surfaces of a light absorber in photocatalytic overall water splitting in nearly pH neutral solutions,[4-6] such as pure water or seawater, thereby promising large scale practical application. Direct photocatalytic water splitting has stringent requirements on the electronic band structures of the semiconductor light absorbers:[5, 7] the conduction and valence band edges must straddle water redox potentials with sufficient chemical overpotentials for proton reduction and water oxidation reactions, respectively,[8-10] while the energy bandgap should be sufficiently narrow for efficient sunlight harvesting. In spite of intensive studies on photocatalytic water splitting,[6, 11-15] most of the semiconductor light absorbers reported to date do not possess suitable band edge positions for overall water splitting under visible light illumination.[16-18] For example, metal oxides, such as TiO_2, $InNiTaO_4$, $SrTiO_3$, GaN/ZnO, and $LaMgTaO_2$,[14, 19-23] can only absorb a small part of solar spectra due to their large bandgaps, whereas narrow bandgap semiconductors, such as Si, GaAs, and InP, [24-26] do not possess suitable band edge positions to drive overall water splitting. Intensive studies have been performed to extend the energy bands of various wide bandgap materials to enhance the efficiency of photocatalytic solar water splitting, such as black TiO_2 by metal doping, dye sensitization, or adding surface hydroxyl groups, but with limited success.[27-31] To date, the solar-to-hydrogen (STH) conversion efficiency is generally limited to <0.5% for single-band metal-oxide photocatalysts (see Supplementary Table S1). An STH efficiency up to 5% has been reported with the use of CoO_x

nanoparticles but the stability is limited to ~30 mins.[4] Z-scheme photocatalytic systems using two-step photo-excitation, in principle, can overcome the unsuitable energy band structures for water redox reactions. For example, $SrTiO_3/BiVO_4$ has been studied for improved photocatalytic performance.[11, 32] However, the energy conversion efficiency is still limited to ~1% (see Supplementary Table S1).

Recently, metal-nitride semiconductors, *e.g.,* $In_xGa_{1-x}N$ (noted as InGaN), have drawn significant attention for photocatalytic water splitting.[33-38] The energy gap of InGaN materials can be continuously varied from ultraviolet, through the visible, to the near-infrared, covering nearly the entire solar spectra. Significantly, the energy band edge positions of InGaN materials can straddle water redox potentials for a large range of alloy compositions (up to indium compositions ~40-50%), which corresponds to an energy bandgap ~1.7-2 eV.[39-41] GaN-based materials have also been widely used in electronics and photonics industries, being the 2nd most produced semiconductor (next to only silicon).[42] Since the first demonstration of photocatalytic overall water splitting on GaN nanostructures, significantly improved performance has been reported by engineering the surface charge properties through p-type dopant incorporation and surface Fermi level tuning.[30, 43, 44] The wide bandgap (~3.4 eV) of GaN, however, greatly limits its light absorption capacity only in the ultraviolet. To enhance its visible light absorption, InGaN can be integrated forming the double-band structure as demonstrated previously.[33, 45] In addition, the Mg doping gradient in III-nitride nanostructures can form a built-in electric field facilitating charge carrier separation and extraction.[34, 41] Recently, photocatalytic overall water splitting with an STH efficiency up to 3.3% has been demonstrated with the use of double-band InGaN/GaN nanowire structures.[33, 34] However, in these studies, the

indium composition is limited to ~22% or less, corresponding to an energy gap >2.6 eV, which can only absorb photons in the blue spectrum. Albeit photocatalytic water splitting with photon absorption up to 560 nm has been reported for InGaN nanowire photocatalyst,[46, 47] the reported efficiency is still very low, largely due to the inefficient separation and extraction of photo-generated charge carriers.

In this work, we have investigated the design and performance of multi-band InGaN/GaN nanowire arrays for photocatalytic overall pure water splitting. The monolithically integrated quadruple-band InGaN nanowire photocatalyst consists of Mg-doped (p-type) $In_{0.35}Ga_{0.65}N$ (E_g ~2.1 eV), $In_{0.27}Ga_{0.73}N$ (E_g ~2.4 eV), $In_{0.20}Ga_{0.80}N$ (E_g ~2.6 eV) and GaN (E_g ~3.4 eV) segments, which were grown on nonplanar silicon wafers by plasma-assisted molecular beam epitaxy (MBE) and can effectively absorb ultraviolet and visible portion of the solar spectra. The use of a nonplanar Si wafer allows for the controlled formation of an Mg doping gradient along the lateral dimension of the nanowire structure. The resulting built-in electric field steers photo-generated electrons and holes to the proton reduction and water oxidation sites, respectively, thereby leading to more efficient charge carrier separation and suppressed the recombination and back reaction. An STH conversion efficiency of ~5.2% was achieved on such quadruple-band InGaN nanowire photocatalyst. The artificial photosynthesis device presented in this study offers a unique platform for achieving high efficiency, scalable solar-to-fuel conversion, including solar water splitting and reduction of carbon dioxide (CO_2) to hydrocarbon fuels.

Illustrated in Figure 1a is the schematic conduction and valence band edge positions of GaN, $In_{0.4}Ga_{0.6}N$, and InN, and their respective alignments to the water redox potentials, represented by hydrogen evolution reaction (HER) and oxygen evolution reaction (OER)

in pH neutral water solution.[48-50] It is seen that InGaN alloys with indium compositions up to ~40% can meet the stringent electronic and thermodynamic requirements for overall water splitting and therefore have the potential to drive solar water splitting in pH neutral electrolyte solutions without sacrificial reagents.[49, 50] The overall photocatalytic water splitting system presented in this study is illustrated in Figure 1b, showing the monolithic integration of InGaN nanowire arrays on a nonplanar silicon wafer. Schematic of the ideal configuration for quadruple-band InGaN nanowire structure and light splitting diagram is further depicted in Figure 1c. Indium compositions in each band are 0%, ~20%, ~27%, and ~35% in this study, corresponding to energy bandgaps of ~3.4 eV, ~2.6 eV, ~2.4 eV, and ~2.1 eV, respectively, which could absorb solar photons with wavelengths up to ~600 nm. For comparison, previously reported photocatalytic devices can only absorb high energy photons (2.8~3.5 eV) for overall water splitting,[41, 51, 52] which limits their energy conversion efficiencies. In addition, the use of a nonplanar wafer in this work offers several benefits. It leads to enhanced light trapping and absorption,[53, 54] and allows for the direct exposure of lateral surfaces of nanowire arrays to normal sunlight illumination. As such, an inverted multi-band structure is studied, with the narrower bandgap light absorber placed atop. Schematically shown in Figure 1d is the monolithically integrated quadruple-band $In_{0.35}Ga_{0.65}N/In_{0.27}Ga_{0.73}N/In_{0.20}Ga_{0.80}N/GaN$ nanowire structure used for photocatalytic overall water splitting in this study. Such a stacking sequence was found to be easier to grow by plasma-assisted MBE (see Methods).

Significantly, due to the use of a nonplanar Si wafer and the formation of nanowires vertically aligned to the local surfaces (Figure 1b), only one side of the nanowires is directly exposed to Mg doping flux during nanowire epitaxial growth, schematically shown in

Figure 1d. As such, an Mg doping gradient is spontaneously formed along the nanowire lateral dimension, which introduces a built-in electric field, shown in Figure 1e.[34] It is seen that photo-generated electrons migrate towards the lightly Mg-doped side for proton reduction reaction, whereas photo-generated holes drift to the more heavily Mg-doped surface for water oxidation reaction. The rapid separation and extraction of photo-generated electrons and holes to the respective cathodic and anodic surfaces can significantly reduce charge carrier recombination and further suppress any back reaction, thereby leading to enhanced efficiency for solar water splitting.[55-58]

Scanning electron microscope (SEM) images of metal-nitride nanowires grown on planar and nonplanar Si wafers are shown in Figures 2a and 2b, respectively. InGaN nanowires grown on a nonplanar Si wafer improve the hydrophilic property, shown in Supplementary Figure S1, which may promote more efficient mass diffusion during solar water splitting. Strong photoluminescence (PL) emission spectra of single-band InGaN nanowires with various indium compositions were measured at room temperature, shown in Figure 2c, confirming the excellent material quality. By varying the growth conditions (see Methods), their energy bandgaps can be tuned from ~3.4 eV to ~2.1 eV, corresponding to PL emission wavelengths from ~370 nm to ~580 nm, respectively.[39, 59, 60] For the PL emission at ~580 nm, the corresponding indium composition is ~35% (see Supplementary Figure S2).[42]

We have first performed photocatalytic water splitting studies on individual single-band InGaN nanowire photocatalyst with varied indium compositions and Mg-dopant incorporations (see Methods). The photocatalytic water splitting performance of p-$In_{0.20}Ga_{0.80}N$, p-$In_{0.27}Ga_{0.73}N$, and p-$In_{0.35}Ga_{0.65}N$ nanowires are summarized in Figures 2d-

f, respectively. Recent studies suggest that Mg doping plays a critical role on the photocatalytic performance of III-nitride materials for overall solar water splitting.[30, 61] Therefore, we have firstly investigated and optimized the Mg doping effect on solar hydrogen gas production by varying the Mg doping flux (controlled by the Mg effusion cell temperature). The optimum Mg cell temperatures were identified to be ~265 ^{o}C, 260 ^{o}C, and 250 ^{o}C for $In_{0.20}Ga_{0.80}N$, $In_{0.27}Ga_{0.73}N$, and $In_{0.35}Ga_{0.65}N$ nanowire photocatalyst, respectively. An optimum level of Mg dopant concentration is required to minimize the surface band bending for the efficient extraction of photo-generated charge carriers, as reported previously.[30, 34, 61] The optimum Mg doping levels, however, depend on indium composition and growth conditions (see Methods). In addition, 20-40% higher hydrogen production rate was measured for InGaN photocatalysts grown on nonplanar Si wafers compared to those on planar Si wafers under optimized conditions, due to, in part, the enhanced charge carrier separation and extraction (Figure 1e). The photocatalytic performance for InGaN nanowires under visible light irradiation has been further confirmed by utilizing various long-pass filters (see Supplementary Figure S3).

We have subsequently studied quadruple-band metal-nitride nanowire photocatalyst by monolithically integrating p-$In_{0.35}Ga_{0.65}N$, p-$In_{0.27}Ga_{0.73}N$, and p-$In_{0.20}Ga_{0.80}N$ together on p-GaN segment (see Figure 1d), which can absorb incident light with wavelengths up to ~600 nm. Prior to the demonstration of quadruple-band structure, we first studied the photocatalytic performance of triple-band metal-nitride nanowires for overall solar water splitting (see Supplementary Note S1 and Supplementary Figure S4). Shown in Figure 3a are the SEM images of quadruple-band InGaN nanowires grown on a nonplanar Si substrate. The flower-shaped morphology of InGaN nanostructures can maximize the side

surface exposed to incident light illumination. The multi-band InGaN nanowires were further characterized by scanning transmission electron microscopy (STEM) and energy-dispersive X-ray spectroscopy (EDX). Shown in Figure 3b, the brighter contrast in the top region of the nanowire indicates more indium incorporation due to the atomic number contrast nature in high angle annular dark-field (HAADF) imaging. The InGaN nanowire becomes wider in diameter along the growth direction (indicated by the white arrow). EDX line scans were performed along axial and lateral directions of the InGaN nanowire. Variations of Ga Lα, In Lα, and N Kα characteristic signals are presented in Figures 3c, 3d, 3e, and 3f for EDX scans along Line 1, Line 2, Line 3, and Line 4 in Figure 3b, respectively. Along the axial direction, In Lα signal intensity gradually decreases, indicating the reduced concentration of In incorporation from top to bottom of the InGaN nanowire, corresponding to the design shown in Figure 1d. There are four segments forming such quadruple-band InGaN nanowire, including (I) $In_{0.35}Ga_{0.65}N$, (II) $In_{0.27}Ga_{0.63}N$, (III) $In_{0.20}Ga_{0.80}N$, and (IV) GaN. For each InGaN segment, variations of Ga Lα and In Lα characteristic signal along the nanowire lateral dimensions are measured and shown in Figures 3d, 3e, and 3f, respectively. We have further performed atomic resolution HAADF-STEM imaging for InGaN crystals with various indium compositions, shown in Figures 3g-i. The periodic ordering of atoms further demonstrates the high crystallinity, which is critical to reduce the bulk recombination for efficient charge carrier extraction.

Schematically illustrated in Figure 4a is the overall solar water splitting process on such quadruple-band InGaN nanowire photocatalyst under light illumination, including photon excitation in each single-band segment, charge carrier separation and extraction, and catalytic water splitting reaction. Due to the built-in electric field introduced by the Mg

doping gradient profile, photo-generated electrons and holes are efficiently separated towards the cathodic surface driving water reduction reaction and anodic surface driving water oxidation reaction, respectively.[34, 57] Furthermore, Supplementary Figure S5 demonstrates the separate deposition of Rh and CoO_x co-catalyst nanoparticles on the lightly and heavily Mg-doped InGaN surfaces, respectively, which indicates efficient charge carrier separation and extraction due to the Mg doping gradient along the lateral dimension of the nanowires. The rapid separation and extraction of photo-generated electrons and holes to the respective cathodic and anodic surfaces can significantly reduce charge carrier recombination and further suppress any back reaction.[55-58] Shown in Figure 4b is the PL spectrum of quadruple-band InGaN nanowires measured at room-temperature. The very broad emission spectrum indicates its capability of absorbing solar photons across nearly the entire visible spectrum. PL emission spectra of individual InGaN segments are also shown in Figure 4b for comparison.

Photocatalytic water splitting measurements of the quadruple-band nanowire arrays were performed in pH ~7 pure water solution under concentrated light illumination using an AM 1.5G filter (see Methods). Shown in Figure 4c is the H_2 and O_2 gas evolution for 120 minutes continuous solar water splitting. Multiple cycles of photocatalytic experiments were further performed to confirm the stable, continuous gas production. The calculated H_2 to O_2 production ratio is nearly 2:1, corresponding to the stoichiometric ratio in water molecules (H_2O), which is consistent with overall water splitting reaction occurring without other byproduct.[5] The H_2 generation rate was measured to be ~1840 μmol cm^{-2} h^{-1} corresponding to an STH efficiency ~5.2% (see Supplementary Note S2).

Summarized in Supplementary Table S1 is the performance comparison of some previously best-reported photocatalyst systems for overall solar water splitting, compared to the quadruple-band InGaN nanowire photocatalyst demonstrated in this work. To date, for III-nitride semiconductors, the best reported STH efficiency is 3.3% on double-band $In_{0.22}Ga_{0.78}N$/GaN photochemical diode.[34, 41, 45] For metal oxide and other nitride semiconductors showing comparable photocatalytic stability, *e.g.,* $SrTiO_3$, $BiVO_4$, and C_3N_4,[11, 12, 32, 62-64] the highest STH efficiency has generally been limited to ~1% mainly due to insufficient light absorption and strong recombination. Compared to previously reported CoO_x particulate system with ~30 mins stability,[4] the presented quadruple-band metal-nitride nanowires demonstrate relatively good stability during overall solar water splitting, without showing any significant degradation of photocatalytic performance for ~8 hrs. Compared to previously reported III-nitride photocatalysts, the significantly improved performance is attributed to the following factors: 1) the use of quadruple-band structure to enhance visible light absorption and water redox reaction, 2) the use of nonplanar wafer to enhance light absorption and trapping effect, and 3) controlled p-type dopant incorporation to enhance charge carrier separation and extraction. Theoretically, the ideal multi-band photocatalytic system in the current design can potentially reach an maximum energy conversion efficiency ~16% if all the incident photons above the energy bandgap can be converted to charge carriers to drive water splitting reaction (see Supplementary Figure S6).[65, 66] Therefore, such multi-band nanostructures can be further optimized to achieve a possible STH efficiency >10%, which may include (1) optimization of the design by placing large energy gap materials on top, (2) optimization of the deposition of co-catalyst particles, (3) integration of such nanowire photocatalysts on reflective substrate

surface to further enhance light absorption, and (4) minimization of surface recombination by surface treatment or passivation.

In summary, we have demonstrated wafer-level broadband InGaN nanowire photocatalysts that can significantly improve the efficiency of direct photocatalytic overall water splitting. Such photocatalyst materials can be synthesized on low cost, large area Si wafers utilizing industry standard manufacturing process. Therefore, their large-scale manufacturability is unquestionable in the future. Significantly, with the incorporation of suitable co-catalysts, such a unique structure can be exploited to achieve high efficiency, stable artificial photosynthesis including one-step CO_2 reduction to hydrocarbon fuels.[41, 67-79]

Methods

Nonplanar Si surface preparation. Two-inch prime-grade polished silicon wafer was etched in 80 °C KOH solution (1.8% KOH in weight with 20% isopropanol in volume) for 30 minutes to form the micro-textured surface with Si pyramids.[42] After being neutralized in concentrated hydrochloric acid, surface cleaning by acetone/methanol, and native oxide removal by 10% hydrofluoric acid, the nonplanar Si wafer was loaded into MBE chamber for the growth of InGaN nanowires.

Molecular beam epitaxial growth of multi-band InGaN nanowires. Mg doped (p-type) InGaN nanowires, single-band or multi-band structures, were grown on as-prepared nonplanar Si substrates by plasma-assisted molecular beam epitaxy (MBE) under N-rich conditions. The growth parameters include a gallium (Ga) beam equivalent pressure of ~7E-8 Torr, a nitrogen flow rate of 1 sccm, and a plasma power of 350 W. The substrate temperature, indium (In) beam equivalent pressure (BEP), and magnesium (Mg) cell temperature were tuned to synthesize different single-band or multi-band InGaN nanowires with various p-doping and alloy concentrations. For the single-band p-GaN nanowires, the substrate temperature was 685 ^{o}C, Ga BEP was ~7E-8 Torr. p-Type doping level was tuned by using different Mg cell temperatures. For the single-band p-$In_{0.20}Ga_{0.80}N$ nanowires, the substrate temperature was 675 ^{o}C, Ga BEP ~7E-8 Torr, and In BEP was ~7.3E-8. For single-band p-$In_{0.27}Ga_{0.73}N$ nanowires, the substrate temperature was 662 ^{o}C, Ga BEP was ~7E-8 Torr, and In BEP was ~7.3E-8. For single-band p-$In_{0.35}Ga_{0.65}N$ nanowires, the substrate temperature was 640 ^{o}C with Ga BEP ~7E-8 Torr and In BEP ~3.5E-8. For quadruple-band InGaN nanowires, the growth conditions are similar to those of the constituting single-band nanowires but with varying thicknesses for each segment. It is

worthwhile mentioning that the substrate temperature here refers to the thermocouple reading of the substrate heater, which may be somewhat different from the real substrate surface temperature, depending on the sample size, substrate holder, and mounting configuration.

Cocatalyst nanoparticle deposition. Prior to photocatalytic water splitting experiments, metal nitride nanowires were decorated with hydrogen evolution reaction (HER) and oxygen evolution reaction (OER) cocatalyst nanoparticles for efficient water redox reactions using photo-deposition method. InGaN samples were put in a glass chamber with a quartz lid, which was first pumped down and then illuminated using a 300 W Xenon lamp for 20 minutes to deposit cocatalyst nanoparticles on InGaN nanowires. The deposition of Rh/CrO_x core/shell structures consists of two steps, including 1) the use of 55 ml deionized water, 11 mL methanol, and 2 μmol sodium hexachlororhodate (Na_3RhCl_6, Sigma-Aldrich) for the formation of Rh core, and 2) the use of 55 mL deionized water, 11 mL methanol, and 4 μmol potassium chromate (K_2CrO_4, Sigma-Aldrich) for CrO_x shell. The deposition of CoO_x nanoparticles involves the use of 60 mL deionized water, 6 mL potassium iodate (KIO_3, 0.01 M, Sigma-Aldrich), and 4 μmol cobalt nitrate ($Co(NO_3)_2$, Alfa Aesar).

Photocatalytic water splitting measurements. Photocatalytic overall water splitting measurements were conducted in a vacuum chamber with a quartz lid. The measurement chamber was partially filled with 70 mL pure water solution (pH ~7), which covered the InGaN photocatalysts, and then was pumped down. After evacuating the chamber, the sample was illuminated with a Xenon lamp (PE300BUV, CERMAX) together with various optical filters. With the use of AM 1.5G filter, the light intensity is ~ 2339 mW/cm^2, equivalent to ~23 suns, as measured at the sample position. The water solution was purged

using argon gas for 30 minutes before any experiments. H_2 and O_2 gas was analyzed by sampling using a vacuum-tight syringe and evaluating using a gas chromatograph machine (GC-8A, Shimazdu) equipped with a thermal conductivity detector (TCD) and high purity argon as carrier gas. The sample size is in the range of 0.5~1 cm^2 for photocatalytic experiments.

Structural and optical characterization. Room-temperature photoluminescence measurements of InGaN nanowires were performed in a homemade setup with a He-Cd 325 nm laser as the excitation source, and the emission is spectrally resolved by a SPEX spectrometer equipped with a photomultiplier tube. SEM images were recorded with a secondary electron detector using a Tescan MIRA3 system (15 kV) and a JEOL IT500 system (20 kV) with an EDX detector. High angle annular dark-field scanning transmission electron microscopy (HAADF-STEM) images were collected using a JEOL 3100R05 microscope operated at 300 keV in aberration corrected STEM mode with a beam convergence angle 22 mrad and detector collection angle 85 mrad.

Acknowledgements

This work was supported by National Science Foundation under grant CBET 1804458. This work was performed in part at the University of Michigan Lurie Nanofabrication Facility. The authors acknowledge financial support from the University of Michigan College of Engineering and technical support from the Michigan Center for Materials Characterization. The authors sincerely acknowledge the assistance from Mr. Yazhou Zhang at Xi'an Jiaotong University, China for photocatalytic pure water splitting experiments on Mg doping optimization of single-band metal nitride nanowires.

Additional information

Supplementary Information is available at XX.

The authors declare no competing interests.

References

1 A. Fujishima; K. Honda, *Nature*, 1972, **238**, 37.

2 X. Chen; S. Shen; L. Guo; S. S. Mao, *Chem. Rev.*, 2010, **110**, 6503-6570.

3 C. F. Shih; T. Zhang; J. Li; C. Bai, *Joule*, 2018.

4 L. Liao; Q. Zhang; Z. Su; Z. Zhao; Y. Wang; Y. Li; X. Lu; D. Wei; G. Feng; Q. Yu; X. Cai; J. Zhao; Z. Ren; H. Fang; F. Robles-Hernandez; S. Baldelli; J. Bao, *Nat. Nanotechnol.*, 2013, **9**, 69.

5 Y. Wang; S. Zhao; Y. Wang; D. A. Laleyan; Y. Wu; B. Ouyang; P. Ou; J. Song; Z. Mi, *Nano Energy*, 2018, **51**, 54-60.

6 Z. Wang; Y. Inoue; T. Hisatomi; R. Ishikawa; Q. Wang; T. Takata; S. Chen; N. Shibata; Y. Ikuhara; K. Domen, *Nat. Catal.*, 2018.

7 K. Takanabe, *ACS Catal.*, 2017, **7**, 8006-8022.

8 B. A. Pinaud; J. D. Benck; L. C. Seitz; A. J. Forman; Z. Chen; T. G. Deutsch; B. D. James; K. N. Baum; G. N. Baum; S. Ardo; H. Wang; E. Miller; T. F. Jaramillo, *Energy Environ. Sci.*, 2013, **6**, 1983-2002.

9 M. Grätzel, *Nature*, 2001, **414**, 338.

10 L. Yuan; C. Han; M.-Q. Yang; Y.-J. Xu, *Int. Rev. Phys. Chem.*, 2016, **35**, 1-36.

11 Q. Wang; T. Hisatomi; Q. Jia; H. Tokudome; M. Zhong; C. Wang; Z. Pan; T. Takata; M. Nakabayashi; N. Shibata; Y. Li; I. D. Sharp; A. Kudo; T. Yamada; K. Domen, *Nat. Mater.*, 2016, **15**, 611.

12 J. Liu; Y. Liu; N. Liu; Y. Han; X. Zhang; H. Huang; Y. Lifshitz; S.-T. Lee; J. Zhong; Z. Kang, *Science*, 2015, **347**, 970.

13 K. Maeda; K. Teramura; D. Lu; T. Takata; N. Saito; Y. Inoue; K. Domen, *Nature*, 2006, **440**, 295.

14 Z. Zou; J. Ye; K. Sayama; H. Arakawa, *Nature*, 2001, **414**, 625.

15 S.-H. Li; N. Zhang; X. Xie; R. Luque; Y.-J. Xu, *Angew. Chem. Int. Ed.*, 2018, **57**, 13082-13085.

16 S. Y. Tee; K. Y. Win; W. S. Teo; L.-D. Koh; S. Liu; C. P. Teng; M.-Y. Han, *Adv. Sci.*, 2017, **4**, 1600337.

17 A. Kudo; Y. Miseki, *Chem. Soc. Rev.*, 2009, **38**, 253-278.

18 S. Liu; C. Han; Z.-R. Tang; Y.-J. Xu, *Mater. Horiz.*, 2016, **3**, 270-282.

19 M. Ge; Q. Li; C. Cao; J. Huang; S. Li; S. Zhang; Z. Chen; K. Zhang; S. S. Al-Deyab; Y. Lai, *Adv. Sci.*, 2016, **4**, 1600152.

20 Y. Goto; T. Hisatomi; Q. Wang; T. Higashi; K. Ishikiriyama; T. Maeda; Y. Sakata; S. Okunaka; H. Tokudome; M. Katayama; S. Akiyama; H. Nishiyama; Y. Inoue; T. Takewaki; T. Setoyama; T. Minegishi; T. Takata; T. Yamada; K. Domen, *Joule*, 2018, **2**, 509-520.

21 S. P. Phivilay; C. A. Roberts; A. D. Gamalski; E. A. Stach; S. Zhang; L. Nguyen; Y. Tang; A. Xiong; A. A. Puretzky; F. F. Tao; K. Domen; I. E. Wachs, *ACS Catal.*, 2018, **8**, 6650-6658.

22 Z. Pan; T. Hisatomi; Q. Wang; S. Chen; A. Iwase; M. Nakabayashi; N. Shibata; T. Takata; M. Katayama; T. Minegishi; A. Kudo; K. Domen, *Adv. Func. Mater.*, 2016, **26**, 7011-7019.

23 S. Liu; Z.-R. Tang; Y. Sun; J. C. Colmenares; Y.-J. Xu, *Chem. Soc. Rev.*, 2015, **44**, 5053-5075.

24 Y. H. Lee; J. Kim; J. Oh, *ACS Appl. Mater. Interfaces*, 2018, **10**, 33230-33237.

25 R. Fan; G. Huang; Y. Wang; Z. Mi; M. Shen, *Appl. Catal. B*, 2018, **237**, 158-165.

26 M. H. Lee; K. Takei; J. Zhang; R. Kapadia; M. Zheng; Y.-Z. Chen; J. Nah; T. S. Matthews; Y.-L. Chueh; J. W. Ager; A. Javey, *Angew. Chem. Int. Ed.*, 2012, **51**, 10760-10764.

27 R. Chen; S. Pang; H. An; J. Zhu; S. Ye; Y. Gao; F. Fan; C. Li, *Nat. Energy*, 2018, **3**, 655-663.

28 B. Wang; S. Shen; S. S. Mao, *J. Materiomics*, 2017, **3**, 96-111.

29 C. Pan; T. Takata; M. Nakabayashi; T. Matsumoto; N. Shibata; Y. Ikuhara; K. Domen, *Angew. Chem. Int. Ed.*, 2015, **54**, 2955-2959.

30 M. G. Kibria; S. Zhao; F. A. Chowdhury; Q. Wang; H. P. T. Nguyen; M. L. Trudeau; H. Guo; Z. Mi, *Nat. Commun.*, 2014, **5**, 3825.

31 N. Zhang; C. Han; Y.-J. Xu; J. J. Foley Iv; D. Zhang; J. Codrington; S. K. Gray; Y. Sun, *Nat. Photonics*, 2016, **10**, 473.

32 Q. Wang; T. Hisatomi; Y. Suzuki; Z. Pan; J. Seo; M. Katayama; T. Minegishi; H. Nishiyama; T. Takata; K. Seki; A. Kudo; T. Yamada; K. Domen, *J. Am. Chem. Soc.*, 2017, **139**, 1675-1683.

33 X. Guan; F. A. Chowdhury; N. Pant; L. Guo; L. Vayssieres; Z. Mi, *J. Phys. Chem. C*, 2018, **122**, 13797-13802.

34 F. A. Chowdhury; M. L. Trudeau; H. Guo; Z. Mi, *Nat. Commun.*, 2018, **9**, 1707.

35 Y. L. Wang; T. Nie; Y. H. Li; X. L. Wang; L. R. Zheng; A. P. Chen; X. Q. Gong; H. G. Yang, *Angew. Chem. Int. Ed.*, 2017, **56**, 7430-7434.

36 E. Nurlaela; A. Ziani; K. Takanabe, *Mater. Renew. Sustain. Energy*, 2016, **5**, 18.

37 X. Jia; Y. Zhao; G. Chen; L. Shang; R. Shi; X. Kang; G. I. N. Waterhouse; L.-Z. Wu; C.-H. Tung; T. Zhang, *Adv. Energy Mater.*, 2016, **6**, 1502585.

38 T. Ohno; L. Bai; T. Hisatomi; K. Maeda; K. Domen, *J. Am. Chem. Soc.*, 2012, **134**, 8254-8259.

39 T. Kuykendall; P. Ulrich; S. Aloni; P. Yang, *Nat. Mater.*, 2007, **6**, 951.

40 P. G. Moses; M. Miao; Q. Yan; C. G. Van de Walle, *J. Chem. Phys.*, 2011, **134**, 084703.

41 M. G. Kibria; Z. Mi, *J. Mater. Chem. A*, 2016, **4**, 2801-2820.

42 Y. Wang; S. Vanka; J. Gim; Y. Wu; R. Fan; Y. Zhang; J. Shi; M. Shen; R. Hovden; Z. Mi, *Nano Energy*, 2019, **57**, 405-413.

43 M. G. Kibria; H. P. T. Nguyen; K. Cui; S. Zhao; D. Liu; H. Guo; M. L. Trudeau; S. Paradis; A.-R. Hakima; Z. Mi, *ACS Nano*, 2013, **7**, 7886-7893.

44 D. Wang; A. Pierre; M. G. Kibria; K. Cui; X. Han; K. H. Bevan; H. Guo; S. Paradis; A.-R. Hakima; Z. Mi, *Nano Lett.*, 2011, **11**, 2353-2357.

45 X. Guan; F. A. Chowdhury; Y. Wang; N. Pant; S. Vanka; M. L. Trudeau; L. Guo; L. Vayssieres; Z. Mi, *ACS Energy Lett.*, 2018, **3**, 2230-2231.

46 M. G. Kibria; F. A. Chowdhury; M. L. Trudeau; H. Guo; Z. Mi, *Nanotechnology*, 2015, **26**, 285401.

47 S. Rajaambal; M. Mapa; C. S. Gopinath, *Dalton Trans.*, 2014, **43**, 12546-12554.

48 Y. Cui; L. Peng; L. Sun; Q. Qian; Y. Huang, *J. Mater. Chem. A*, 2018, **6**, 22768-22777.

49 P. G. Moses; C. G. Van de Walle, *Appl. Phys. Lett.*, 2010, **96**, 021908.

50 F. A. Chowdhury; Z. Mi; M. G. Kibria; M. L. Trudeau, *APL Mater.*, 2015, **3**, 104408.

51 S. Chen; T. Takata; K. Domen, *Nat. Rev. Mater.*, 2017, **2**, 17050.

52 D.-H. Tu; H.-C. Wang; P.-S. Wang; W.-C. Cheng; K.-H. Chen; C.-I. Wu; S. Chattopadhyay; L.-C. Chen, *Int. J. Hydrog. Energy*, 2013, **38**, 14433-14439.

53 E. Garnett; P. Yang, *Nano Lett.*, 2010, **10**, 1082-1087.

54 L. Meng; Y. Zhang; C. Yam, *J. Phys. Chem. Lett.*, 2017, **8**, 571-575.

55 Q. Shi; S. Murcia-López; P. Tang; C. Flox; J. R. Morante; Z. Bian; H. Wang; T. Andreu, *ACS Catal.*, 2018, **8**, 3331-3342.

56 L. I. Granone; F. Sieland; N. Zheng; R. Dillert; D. W. Bahnemann, *Green Chem.*, 2018, **20**, 1169-1192.

57 R. Marschall, *Adv. Func. Mater.*, 2014, **24**, 2421-2440.

58 F. Le Formal; S. R. Pendlebury; M. Cornuz; S. D. Tilley; M. Grätzel; J. R. Durrant, *J. Am. Chem. Soc.*, 2014, **136**, 2564-2574.

59 R. R. Pelá; C. Caetano; M. Marques; L. G. Ferreira; J. Furthmüller; L. K. Teles, *Appl. Phys. Lett.*, 2011, **98**, 151907.

60 I. Vurgaftman; J. R. Meyer, *J. Appl. Phys.*, 2003, **94**, 3675-3696.

61 M. G. Kibria; F. A. Chowdhury; S. Zhao; B. AlOtaibi; M. L. Trudeau; H. Guo; Z. Mi, *Nat. Commun.*, 2015, **6**, 6797.

62 A. Nakada; S. Nishioka; J. J. M. Vequizo; K. Muraoka; T. Kanazawa; A. Yamakata; S. Nozawa; H. Kumagai; S.-i. Adachi; O. Ishitani; K. Maeda, *J. Mater. Chem. A*, 2017, **5**, 11710-11719.

63 R. Asai; H. Nemoto; Q. Jia; K. Saito; A. Iwase; A. Kudo, *Chem. Commun.*, 2014, **50**, 2543-2546.

64 Y. Wang; F. Silveri; M. K. Bayazit; Q. Ruan; Y. Li; J. Xie; C. R. A. Catlow; J. Tang, *Adv. Energy Mater.*, 2018, **8**, 1801084.

65 J. Juodkazytė; G. Seniutinas; B. Šebeka; I. Savickaja; T. Malinauskas; K. Badokas; K. Juodkazis; S. Juodkazis, *Int. J. Hydrog. Energy*, 2016, **41**, 11941-11948.

66 K. T. Fountaine; H. J. Lewerenz; H. A. Atwater, *Nat. Commun.*, 2016, **7**, 13706.

67 S. Chu; P. Ou; P. Ghamari; S. Vanka; B. Zhou; I. Shih; J. Song; Z. Mi, *J. Am. Chem. Soc.*, 2018, **140**, 7869-7877.

68 J. K. Sheu; P. H. Liao; T. C. Huang; K. J. Chiang; W. C. Lai; M. L. Lee, *Sol. Energy Mater. Sol. Cells*, 2017, **166**, 86-90.

69 Y. Wang; S. Fan; B. AlOtaibi; Y. Wang; L. Li; Z. Mi, *Chem. Eur. J.*, 2016, **22**, 8809-8813.

70 T. Sekimoto; H. Hashiba; S. Shinagawa; Y. Uetake; M. Deguchi; S. Yotsuhashi; K. Ohkawa, *J. Phys. Chem. C*, 2016, **120**, 13970-13975.

71 S. Chu; S. Fan; Y. Wang; D. Rossouw; Y. Wang; G. A. Botton; Z. Mi, *Angew. Chem. Int. Ed.*, 2016, **55**, 14262-14266.

72 B. AlOtaibi; X. Kong; S. Vanka; S. Y. Woo; A. Pofelski; F. Oudjedi; S. Fan; M. G. Kibria; G. A. Botton; W. Ji; H. Guo; Z. Mi, *ACS Energy Lett.*, 2016, **1**, 246-252.

73 Y. Wang; B. AlOtaibi; F. A. Chowdhury; S. Fan; M. G. Kibria; L. Li; C.-J. Li; Z. Mi, *APL Mater.*, 2015, **3**, 116106.

74 T. Sekimoto; S. Shinagawa; Y. Uetake; K. Noda; M. Deguchi; S. Yotsuhashi; K. Ohkawa, *Appl. Phys. Lett.*, 2015, **106**, 073902.

75 B. AlOtaibi; S. Fan; D. Wang; J. Ye; Z. Mi, *ACS Catal.*, 2015, **5**, 5342-5348.

76 S. Yotsuhashi; M. Deguchi; Y. Yamada; K. Ohkawa, *AIP Adv.*, 2014, **4**, 067135.

77 S. Yotsuhashi; M. Deguchi; Y. Zenitani; R. Hinogami; H. Hashiba; Y. Yamada; K. Ohkawa, *Jpn. J. Appl. Phys.*, 2012, **51**, 02BP07.

78 S. Yotsuhashi; M. Deguchi; H. Hashiba; Y. Zenitani; R. Hinogami; Y. Yamada; K. Ohkawa, *Appl. Phys. Lett.*, 2012, **100**, 243904.

79 S. Yotsuhashi; M. Deguchi; Y. Zenitani; R. Hinogami; H. Hashiba; Y. Yamada; K. Ohkawa, *Appl. Phys. Express*, 2011, **4**, 117101.

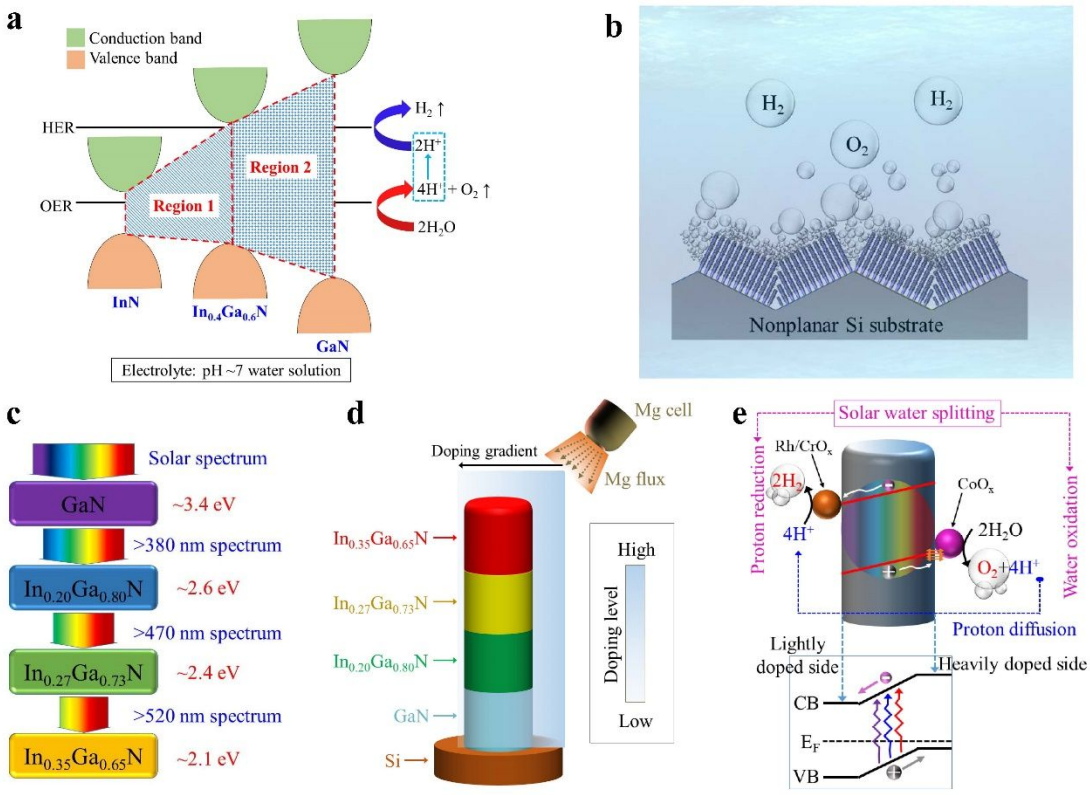

Figure 1. Schematic design and structural properties of monolithic multi-band metal nitride nanowire arrays for photocatalytic overall water splitting in nearly pH neutral electrolyte solution. (a) Band edge positions of GaN, InN, and their InGaN compounds. In pH ~7 liquid solution, InGaN alloys with indium incorporation up to 40% can straddle the water redox reaction, noted as Region 2. Higher indium incorporation (Region 1) makes InGaN compounds unsuitable for overall solar water splitting. (b) Schematic illustration of photocatalytic water splitting on InGaN nanowire arrays monolithically integrated on a nonplanar Si wafer. (c) Schematic illustration of ideal configuration for light absorption on the multi-band InGaN stacks with varied indium compositions. (d) Schematic of the quadruple-band InGaN nanowire. p-Type dopant originating from the tilted Mg effusion cell (relative to the nanowire orientation) leads to the Mg doping gradient profile in lateral direction of the nanowire, which can introduce a built-in electric field, illustrated in (e), for efficient charge carrier separation and extraction for water redox reactions.

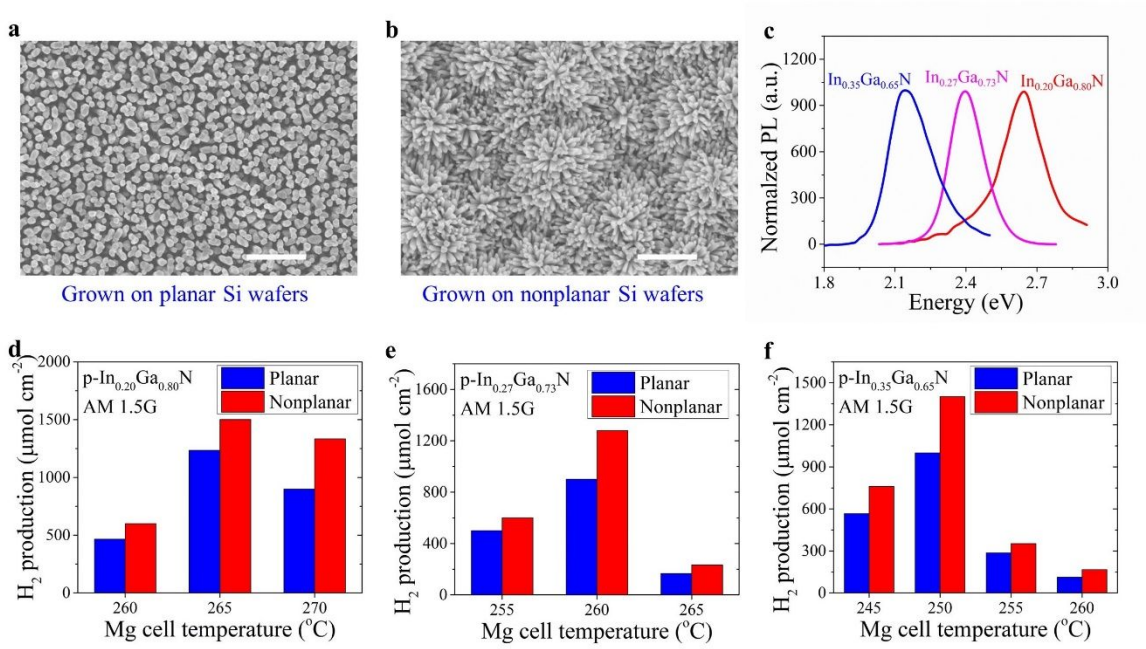

Figure 2. Properties and photocatalytic performance of single-band metal nitride nanowires grown on planar or nonplanar Si wafers, with different doping levels by varying the Mg effusion cell temperature. Electron microscope images of InGaN nanowires grown on planar and nonplanar Si wafers. (a) Scale bar: 1 μm. (b) Scale bar: 1 μm. (c) Room-temperature photoluminescence (PL) spectrum of single-band InGaN nanowires with varied indium compositions of ~20%, ~27%, and ~35%, corresponding to an energy gap of ~2.6 eV, ~2.4 eV, and ~2.1 eV, respectively. (d-f) Summarized H_2 gas production of photocatalytic pure water splitting on single-band p-$In_{0.20}Ga_{0.80}N$ (d), p-$In_{0.27}Ga_{0.73}N$ (e), and p-$In_{0.35}Ga_{0.65}N$ (f) nanowires with varied Mg effusion cell temperatures on planar (blue bar) and nonplanar (red bar) Si wafers. H_2 gas production was recorded after 40 minutes water splitting experiment.

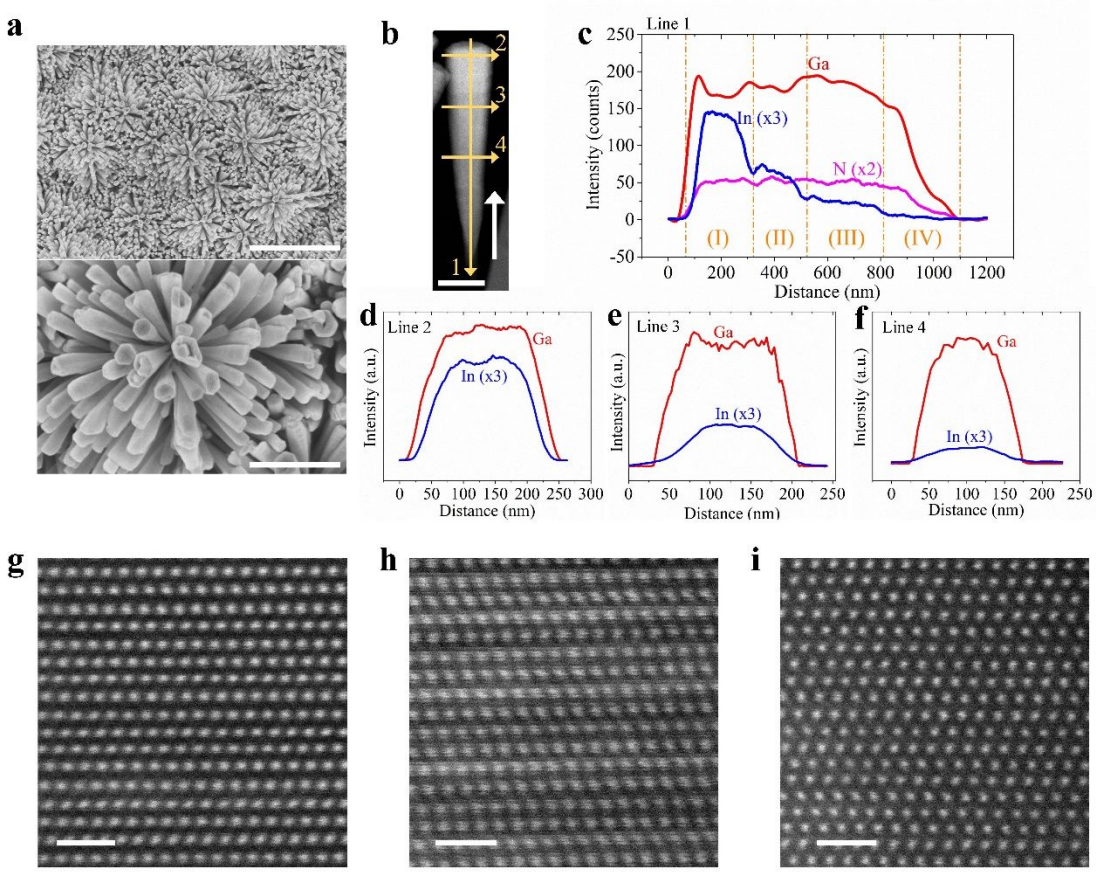

Figure 3. Structural characterization of the quadruple-band InGaN nanowire arrays monolithically integrated on a nonplanar Si wafer. (a) Top-view scanning electron microscope (SEM) images of flower-shaped InGaN nanowire structure grown on nonplanar Si substrates. Scale bar: 5 μm (top) and 1 μm (bottom). (b) Dark-filed scanning transmission electron microscope (DF-STEM) image of quadruple-band InGaN nanowire, with energy-dispersive X-ray spectroscopy (EDX) line scanning showing the variation of Ga Lα, In Lα, and N Kα characteristic signals along the axial and lateral directions. Scale bar: 200 nm. Spectrum of Line 1 (c), Line 2 (d), Line 3 (e), and Line 4 (f) are measured along Arrow 1, Arrow 2, Arrow 3, and Arrow 4 in (b), respectively. (g-i) Atomic resolution STEM images of InGaN crystals for (g) $In_{0.35}Ga_{0.65}N$, (h) $In_{0.27}Ga_{0.73}N$, and (i) $In_{0.20}Ga_{0.80}N$ segment, respectively. Scale bar: 1 nm.

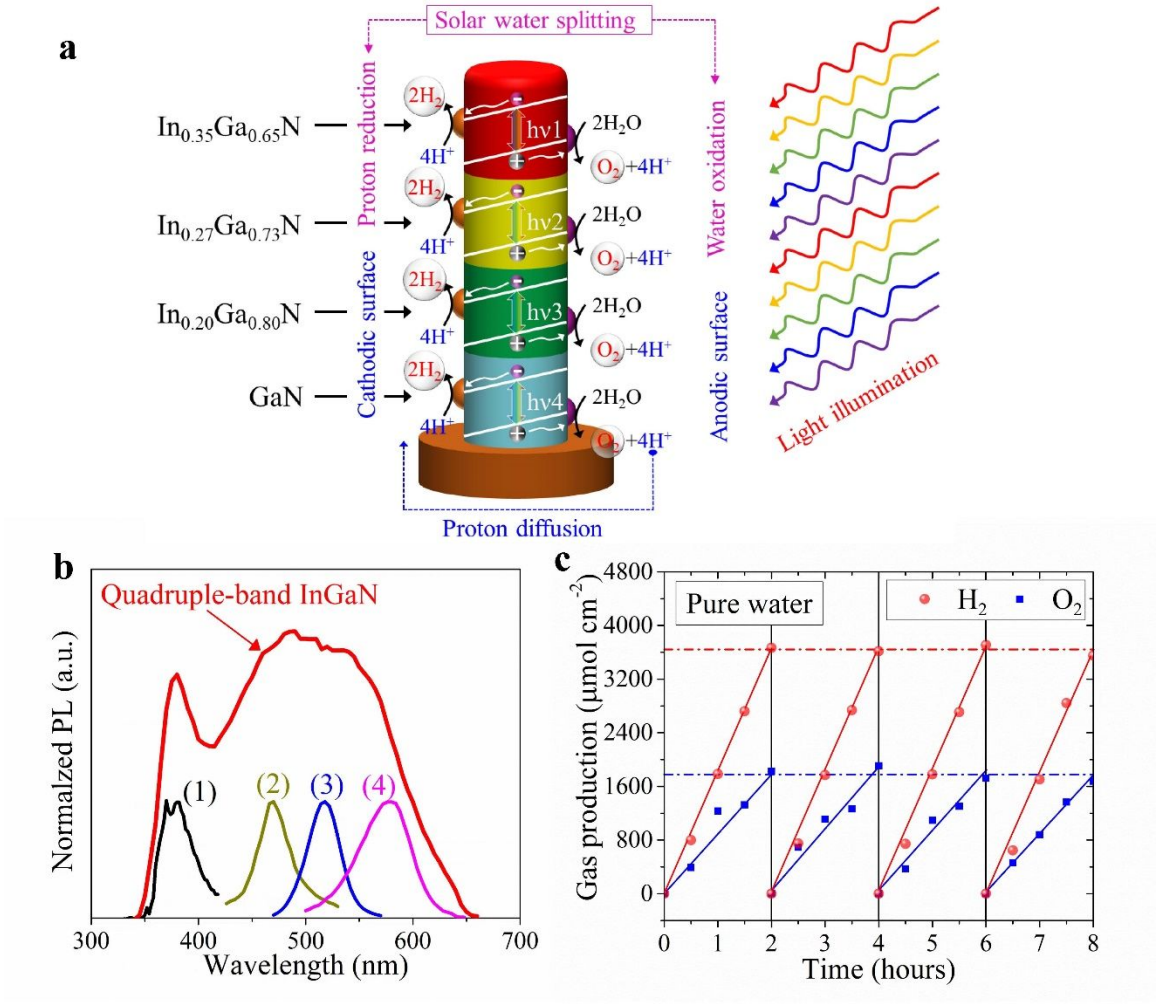

Figure 4. Photocatalytic performance of quadruple-band InGaN nanowire arrays measured in pure water under 300 W Xenon lamp equipped with an AM 1.5G filter. (a) Schematic illustration of overall water splitting process occurring on the quadruple-band nanowires under light illumination. (b) Room-temperature PL spectrum of the quadruple-band InGaN nanowires, compared to those of single-band nanowires, including (1) p-GaN, (2) p-$In_{0.20}Ga_{0.80}N$, (3) p-$In_{0.27}Ga_{0.73}N$, and (4) p-$In_{0.35}Ga_{0.65}N$. (c) H_2 and O_2 gas generation as a function of time measured in multiple experiment cycles.

Table of content

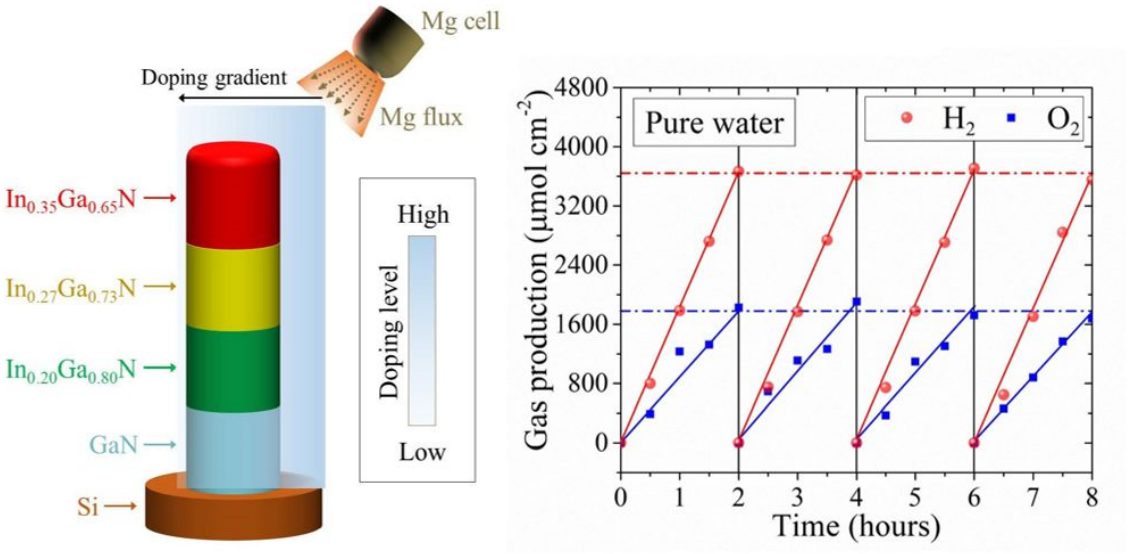

First demonstration of a quadruple-band InGaN nanowire photocatalyst for overall water splitting with an STH efficiency >5%.